# Multiband Dynamics of Extended Harmonic Generation in Solids under Ultraviolet Injection

Yue Lang(郎跃), Zhaoyang Peng(彭朝阳), and Zengxiu Zhao(赵增秀)*

*Department of Physics, National University of Defense Technology, Changsha 410073, China*

(Received 15 September 2022; accepted manuscript online 8 October 2022)

Using one-dimensional semiconductor Bloch equations, we investigate the multiband dynamics of electrons in a cutoff extension scheme employing an infrared pulse with additional UV injection. An extended three-step model is firstly validated to play a dominant role in emitting harmonics in the second plateau. Surprisingly, further analysis employing the acceleration theorem shows that, though harmonics in both the primary and secondary present positive and negative chirps, the positive (negative) chirp in the first region is related to the so-called short (long) trajectory, while that in the second region is emitted through 'general' trajectory, where electrons tunneling earlier and recombining earlier contribute significantly. The novel characteristics deepen the understanding of high harmonic generation in solids and may have great significance in attosecond science and reconstruction of band dispersion beyond the band edge.

DOI: 10.1088/0256-307X/39/11/114201

Highly nonlinear interaction of multicycle laser pulse with gaseous targets enables the generation of high harmonics (HHGs) and lays the foundation of attosecond science.[1] The process of up-converting the fundamental frequency can be well described with the semiclassical three-step model including tunneling, acceleration and recombination[2,3] and has been extensively studied during the past three decades.[4–9] Due to the rich information carried by HHGs from the microcosm, it has been widely applied to the detection of structures and control of ultrafast dynamics with unprecedented spacial and temporal resolutions.[10–20] The cutoff in gases is theoretically and experimentally given by $\hbar\omega_{\rm cutoff} \approx I_{\rm p}+3.17U_{\rm p} \propto I\lambda^2$, illustrating the possibility of extending the energy of harmonic photons well into extreme ultraviolet and even "water window" region employing longer wavelengths.[21–24]

HHGs from solids have also been scrutinized theoretically during the same period,[25–31] partially due to their promise of intenser and higher flux of emission with much denser electrons. However, the experimental observation was reported only recently in zinc oxide,[32] benefiting from longer wavelength of the incident pulse to circumvent radiation damage in condensed materials. Mechanism of solid HHGs still remains under intense debate and is partially shed light on in pump-probe experiments,[33–35] where the rescattering model is found to predict satisfyingly the observations. The high efficiency of HHG in solids replenishes the development of table-top attosecond sources[36] and enables petahertz-bandwidth signal manipulation through ultrafast control of current injection.[37,38] Also, deeper insights into the mechanism of HHGs in solids hold the promises of reconstruction of band structures,[39,40] potential field imaging,[41] detection of topological transition,[42–44] etc. Different from the counterpart in gases, the solid-state cutoff is observed to scale linearly with the electric field[32] and has been demonstrated to depend on the band dispersion,[45] while direct relevance with driving wavelength is still under debate.[46] As a result, potential applications call for deeper understanding of solid HHGs and new methods to extend the cutoff.

Various schemes have been explored intensively to increase the cutoff and intensity of harmonics in solids, such as the employment of solid Ar (or Kr),[36] the consideration of preacceleration,[47] properly doped semiconductor,[48,49] and electron backscattering.[50] On the other hand, different compositions of incident pulses, such as two-color or even three-color ones, have been explored where the relative intensity, delay, carrier-envelope phase (CEP), and pulse shape can be adjusted to achieve better characteristics of resulting harmonic spectra.[51–55] In solids, further extend of harmonics to higher energy region requires intenser incident pulse to drive direct transitions from the highest valence band to higher-lying conduction bands. Due to the large gaps, however, the incident pulse should be intense enough to achieve significant population, which can possibly cause irreversible damage to materials. An appearing bypass is coincidence of infrared (IR) and properly delayed ultraviolet pulses, hereinafter referred to as the IR+UV scheme. We recently have proposed a model to extend the cut-off energy of harmonic generated from solids by injecting both the IR and UV pulses.[56] In this study, we further verify the extended three-step model and discuss the effects of multiple bands. In particular, we examine the difference in the interband dynamics of the two plateaus. In this Letter, first we describe the theoretical model and approaches. Then, we present the extended three-step model and focus on the multiband dynamics in the extended plateau. Finally, we summarize the findings.

*Methods.* The dynamics of electrons in laser solid interaction can be given by the semiconductor Bloch equations

*Corresponding author. Email: zhaozengxiu@nudt.edu.cn
© 2022 Chinese Physical Society and IOP Publishing Ltd

(SBEs):[57–59]

$$i\frac{\partial}{\partial t}\rho_{mn}^{\boldsymbol{k}}(t) = \Big[E_m^{\boldsymbol{k}'} - E_n^{\boldsymbol{k}'} - \frac{i(1-\delta_{mn})}{T_2}\Big]\rho_{mn}^{\boldsymbol{k}}(t) + \boldsymbol{F}(t)\cdot\sum_l\Big[\boldsymbol{d}_{ml}^{\boldsymbol{k}'}\rho_{ln}^{\boldsymbol{k}}(t) - \boldsymbol{d}_{ln}^{\boldsymbol{k}'}\rho_{ml}^{\boldsymbol{k}}(t)\Big], \quad (1)$$

where $\boldsymbol{k}$ is the crystal momentum, $m$ (or $n$) is the band index, $\rho_{mn}$ is the density matrix element, with $m \neq n$ representing the interband polarization and $m = n$ population, $E$ is the band dispersion, $\boldsymbol{F}(t)$ is the electric field, $\boldsymbol{d}$ is the transitional dipole moment (TDM), $T_2$ is the empirical dephasing time, and $\boldsymbol{k}' = \boldsymbol{k} + \boldsymbol{A}(t)$ is the crystal momentum in the moving frame. Note that $T_2$ is set to infinity unless stated otherwise and the influence of shorter dephasing time[60] will be illustrated later.

The total current can be split into the interband and intraband contributions:

$$\boldsymbol{J}_{\text{inter}}(t) = -\int_{\text{BZ}} d\boldsymbol{k}\sum_{m\neq n}\rho_{mn}^{\boldsymbol{k}}\boldsymbol{p}_{nm}^{\boldsymbol{k}}, \quad (2)$$

$$\boldsymbol{J}_{\text{intra}}(t) = -\int_{\text{BZ}} d\boldsymbol{k}\sum_{m=n}\rho_{mn}^{\boldsymbol{k}}\boldsymbol{p}_{nm}^{\boldsymbol{k}}, \quad (3)$$

where the momentum matrix element (MTM) $\boldsymbol{p}_{nm}^{\boldsymbol{k}}$ is related to the TDM $\boldsymbol{d}_{nm}^{\boldsymbol{k}}$ through canonical relation[61]

$$\boldsymbol{d}_{nm}^{\boldsymbol{k}} = \frac{-i\boldsymbol{p}_{nm}^{\boldsymbol{k}}}{E_{\boldsymbol{k}}^n - E_{\boldsymbol{k}}^m} \quad (\text{for } m \neq n). \quad (4)$$

The calculation of one-dimensional band dispersion and TDM are described in other works[57] for model crystal ZnO along $\Gamma$–$M$.

The harmonic spectrum is calculated by Fourier transformation

$$\text{Y}(\omega) = \Big|\int_0^T\Big[\frac{\partial\boldsymbol{J}(t)}{\partial t}w(t)\Big]e^{i\omega t}dt\Big|^2, \quad (5)$$

where $T$ is the calculation time, $w(t)$ is the absorption function given by

$$w(t) = \begin{cases} 1, & t < T_0, \\ e^{\frac{-4\ln 2(t-T_0)^2}{\sigma^2}}, & t \geq T_0, \end{cases} \quad (6)$$

with $T - T_0 \approx 10\,\text{fs}$. Fourier transformation in Eq. (5) is conducted using the fast Fourier transformation (FFT) algorithm.

Time-frequency analysis of the total current is calculated by continuous wavelet transformation

$$\text{S}(t,a) = \Big|\frac{1}{\sqrt{a}}\int_{-\infty}^{\infty}\Big[\frac{\partial}{\partial t'}\boldsymbol{J}(t')\Big]\alpha^*\Big(\frac{t'-t}{a}\Big)dt'\Big|^2, \quad (7)$$

where $a$ is the scale factor, $\alpha(x)$ is the mother wavelet, i.e., Morlet wavelet in our case with the time bandwidth set to 60 to achieve better resolution in time and space, and $\omega$ is related to the central frequency $\Omega$ of the mother wavelet through $\omega = \Omega/a$.

*Results and Discussion.* The general recollision model in two-band approximation[33,34,62] is shown on the right panel of Fig. 1. Near the extreme of electric field, electrons locating initially around high symmetry points are partially excited to the lowest conduction band and form electron hole pairs. Then, electrons (holes) are accelerated by the laser field, with harmonics emitted from intraband current. Finally, when the electric field reverses its direction, excited electrons are driven back towards the holes and complete recombination with emission of harmonics, commonly referred to as the interband mechanism. For direct band-gap materials like ZnO[32] along specific crystal direction, excited electrons locate generally near the center of Brillouin zone (BZ), i.e. $\boldsymbol{k} = 0$, which impedes the following propagation to the band edge to be further pumped to higher-lying band C2.

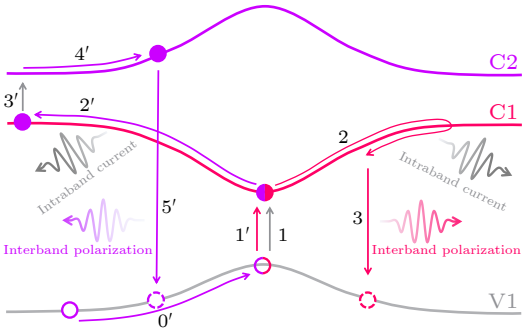


**Fig. 1.** Sketch of the extended three-step model and the general recollision model. Left: acceleration (0′), injection (1′), acceleration (2′), tunneling (3′), acceleration (4′) and recombination (5′). Right: tunneling (1), acceleration (2) and recombination (3). In the extended three-step model, excited electrons on band C2 originate far from the BZ center (magenta solid circle) on band V1, followed by injection to band C1 through properly delayed UV pulse.

The general recollision model in the two-band approximation[33,34,62] is shown on the right side of Fig. 1. Near the extreme of electric field, electrons locating initially around high symmetry points are partially excited to the lowest conduction band and form electron hole pairs. Then, electrons (holes) are accelerated by the laser field, with harmonics emitted from intraband current. Finally, when the electric field reverses its direction, excited electrons are driven back towards the holes and complete recombination with emission of harmonics, commonly referred to as the interband mechanism. For direct band-gap materials like ZnO[32] along specific crystal direction, excited electrons locate generally near the center of Brillouin zone (BZ), i.e., $\boldsymbol{k} = 0$, which impedes the following propagation to the band edge to be further pumped to higher-lying band C2.

In order to extend the cutoff, an additional ultraviolet (UV) pulse can be introduced and the dynamics of electrons are shown on the left side of Fig. 1. Electrons locating initially far from the BZ center are driven by the IR field (step 0′) to the center, followed by excitation to the lowest conduction band C1 through one-photon absorption at the instant of UV injection (step 1′). Then these electrons can be accelerated closer to the BZ boundary (step 2′) and tunnel to band C2 (step 3′) for further acceleration (step 4′). Finally, the electrons on C2 recombine with the hole pairs and emit high energy photons (step 5′). Note that, though the injection scheme has been employed by Sun *et al.*,[55] the motion of electrons in their work is limited to only two bands, which differs from the extended three-step

model.

The pulse shape of both IR and UV is given by

$$F(t) = F_0 \cos^2\left[\pi\Big(\frac{t-t_{\rm delay}}{T} - \frac{1}{2}\Big)\right] \cdot \sin\left[\omega\Big(\frac{t-t_{\rm delay}}{T} - \frac{1}{2}\Big)\right], \quad (8)$$

with $F_0$ being the electric amplitude, $T$ the total duration, $\omega$ the angular frequency and $t_{\rm delay}$ the delay time. The IR pulse is centered at 3200 nm ($\omega_{\rm L} = 0.39$ eV), with a total duration of 8 cycles ($8T_{\rm L}$) and an intensity of $2 \times 10^{11}$W/cm$^2$. The injection UV pulse is centered at 291 nm ($11\omega_{\rm L}$), with a duration of 3 cycles at $-0.25T_{\rm L}$ delay, as shown in the inset of Fig. 2(b). Figure 2(a) illustrates the harmonic spectra at various injection intensities. It can be seen that the cutoff in the IR scheme is $\omega_{\rm cutoff}^{\rm IR} \approx 25\omega_{\rm L}$, while that in the IR+UV scheme is extended to $\omega_{\rm cutoff}^{\rm IR+UV} \approx 60\omega_{\rm L}$ in the secondary plateau.

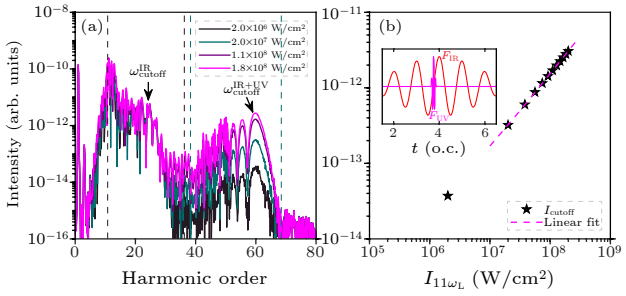


**Fig. 2.** (a) Harmonic spectrum under various injection intensities with IR fixed at $2 \times 10^{11}$W/cm$^2$. The dashed lines represent energy gaps between the highest valence band and the lowest ($11\omega_{\rm L}$ to $36\omega_{\rm L}$) and second lowest ($38\omega_{\rm L}$ to $68\omega_{\rm L}$) conduction band, respectively. Note that the cutoff of IR scheme $\omega_{\rm cutoff}^{\rm IR}$ is obtained by the current driven by the IR field solely and the spectrum has been omitted for clarity. (b) The dependence of cutoff intensity on the injection intensity (dark pentagrams). Inset shows the separately rescaled pulse shape of IR (red) and UV (magenta) fields. Absorption of one UV photon is indicated by the linear fit (magenta dashed line).

Although it is evident that emission in the secondary region origins from significant population on band C2, there are actually three possible channels in the IR+UV setup:

1. V1 to C1 and C1 to C2, both involve the absorption of one UV photon, hereinafter referred to as channel 1.
2. V1 to C1 through absorption of one UV photon and C1 to C2 through tunneling, hereinafter referred to as channel 2.
3. V1 to C1 through tunneling and C1 to C2 through absorption of one UV photon, hereinafter referred to as channel 3.

Through detailed analysis of the intensity dependence and population variation, channel 2 is validated to contribute significantly to the population on C2. Firstly, as shown in Fig. 2(b), the linear dependence of the cutoff intensity on the injection intensity $I_{11\omega_{\rm L}}$ implies that only one UV photon participates in the transition. In result, contribution from channel 1 can be easily omitted for the expected quadratic dependence on UV intensity. In channel 2, i.e., the extended three-step model, it can be predicted that injection at the extreme of electric field fails to populate electrons up to band C2, because additionally excited electrons still locate near the BZ center. Figure 3(a) illustrates the dependence of secondary plateau on the injection delays. As can be seen, only injections near the delay of $-0.25T_{\rm L}$ and $0.25T_{\rm L}$ produce evident radiation. Moreover, Figs. 3(b)–3(d) illustrate the evolution of population variation on band C2 at three typical delays, which show clearly that the excited electrons for the two delays locate initially at $k_0 = -0.6\pi/a_0$ and $0.63\pi/a_0$, respectively, while the injection at zero delay fails to pump electrons to band C2. Finally, because the absorption of one UV photon is needed for transition from C1 to C2 in channel 3, obvious increase of electrons on C2 should be seen at the instant of injection. However, as shown in Figs. 3(b)–3(d), growth of population on C2 is delayed to the instant of UV injection by $0.35T_{\rm L}$. As a result, the extended three-step model is proved to contribute mainly to the generation of harmonics in the secondary plateau.

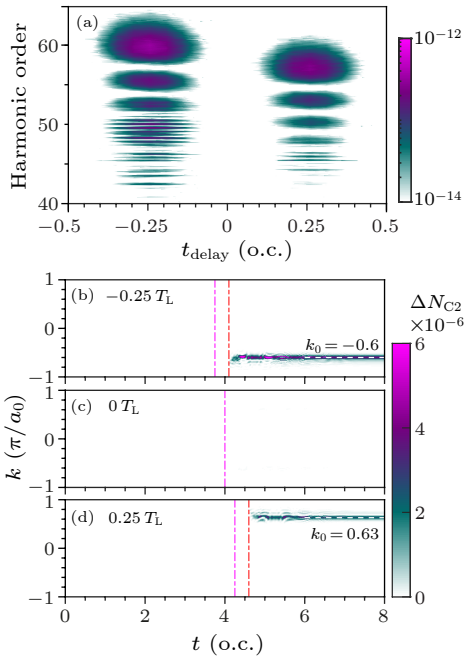


**Fig. 3.** (a) Dependence of harmonic spectrum on two-color delays, with the second plateau presented in logarithmic scale. Population differences of band C2 $\Delta N_{\rm C2}(t,k)$ between the two schemes at the delay of (b) $-0.25T_{\rm L}$, (c) $0T_{\rm L}$ and (d) $0.25T_{\rm L}$, with $\Delta N_{\rm C2}(t,k) = N_{\rm C2}^{\rm IR+UV}(t,k) - N_{\rm C2}^{\rm IR}(t,k)$ are given. The generation of radiation in the extended plateau demands properly delayed UV near the zero-crossing of electric field at $-0.25T_{\rm L}$ or $0.25T_{\rm L}$, and the highly excited electrons on C2 locates far from the center at $k_0 \approx -0.6\pi/a_0$ (white dashed line) and $0.63\pi/a_0$ (white dashed line), respectively, as predicted by the extended three-step model. The emergence of electrons on C2 (red dashed lines) is delayed to the injection instant (magenta dashed line) by $0.35T_{\rm L}$ and proves the failure of channel 3 (see the main text).

Though the transition channel has been validated, the multiband dynamics remain folded so far. Figure 4(a) shows the time-frequency analysis, where harmonic emis-

sion in the primary plateau exhibits clearly a period of half cycle of the fundamental field. The lack of clearness in the spectrum is mainly caused by long dephasing time, which also results in the quantum beat signal at the minimal gap after the end of laser field due to strong coherence of Bloch states near the gap. [63] With the decrease of dephasing time down to $T_{\rm L}$, the beat signal gradually disappears as shown in the inset. Meanwhile, significant emission at $t = 4.75T_{\rm L}$ can also be seen clearly in the second plateau and is delayed by approximately one optical cycle to the injection instant at $3.75T_{\rm L}$. Surprisingly, slightly weakened harmonics are also generated at $t = 6.75T_{\rm L}$, which is emitted by significant recombination of remaining electrons on C2 and can be suppressed by shorter dephasing time as shown in the inset.

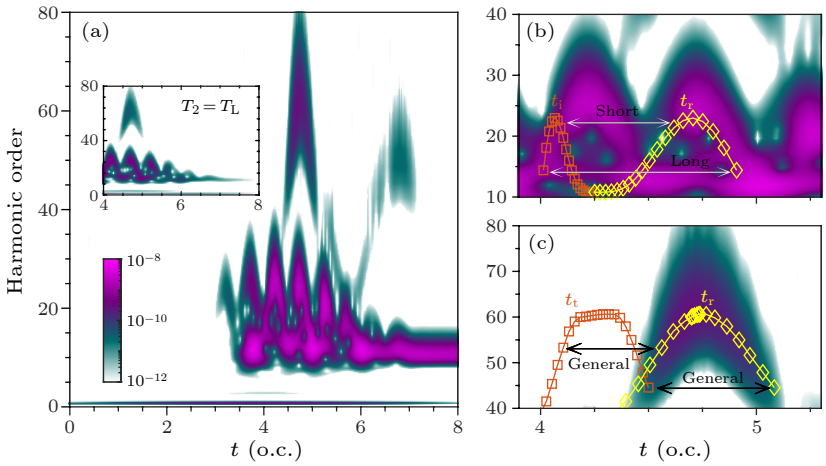


**Fig. 4.** (a) Time-frequency analysis of the two-color delay of $-0.25T_{\rm L}$, with the result of shorter dephasing time $T_2 = T_{\rm L}$ presented in the inset. Strong dephasing leads to obvious suppress of subsequent emissions caused by recombination of excited electrons on C2. Interband dynamics in the (b) first and (c) second plateaus employing the acceleration theorem are present, with $t_{\rm i}$ the ionization instant, $t_{\rm r}$ the recombination time and $t_{\rm t}$ the tunneling instant. Positive chirp in the primary plateau is linked to electrons that ionize later but recombine earlier, i.e., the so-called short trajectory, while that in the secondary plateau is related to electrons that tunnel and recombine earlier, i.e., the 'general' trajectory.

We then examine the subcycle electron dynamics in both the first and second plateaus. Within the acceleration theorem, the spacial displacement of electron hole pairs can be determined by

$$R_{\rm e,h}(t) = \int_{t_{\rm i}}^{t_{\rm r}} \nabla_{\boldsymbol{k}} E[\boldsymbol{k}_0 + A(\tau) - A(t_{\rm i})]d\tau, \tag{9}$$

where $\boldsymbol{k}_0$ is the initial crystal momentum of excited electrons; $t_{\rm i}$ and $t_{\rm r}$ are the ionization and recombination instants, respectively; $t_{\rm r}$ and energy of harmonic $\omega$ are given by

$$R_{\rm e} - R_{\rm h} = 0, \tag{10}$$

$$E_{\rm e}[\boldsymbol{k}_0 + A(t_{\rm r}) - A(t_{\rm i})] - E_{\rm h}[\boldsymbol{k}_0 + A(t_{\rm r}) - A(t_{\rm i})] = \hbar\omega. \tag{11}$$

Taking ionization near $4T_{\rm L}$ as an example, Fig. 4(b) shows the dependence of harmonic energy and recombination time on ionization time by solving Eqs. (9)–(11) with $\boldsymbol{k}_0 = 0$. It can be seen that electrons ionized right after the field extreme ($4T_{\rm L} \leq t \leq 4.06T_{\rm L}$) recombine at delays larger than $\sim 0.7T_{\rm L}$, while those ionized later ($4.06T_{\rm L} < t \leq 4.25T_{\rm L}$) recombine earlier, i.e., the so-called long and short trajectories, respectively. Meanwhile, emissions from long trajectory exhibit negative chirp while those from short trajectory generate positive chirp. Similarly, the displacement of electrons in the extended three-step model is given by a convenient variation of Eq. (9) as follows:

$$R_{\rm e}(t) = \int_{t_{\rm i}}^{t_{\rm t}} \nabla_{\boldsymbol{k}} E_{\rm C1}[\boldsymbol{k}_0 + A(\tau) - A(t_{\rm i})]d\tau + \int_{t_{\rm t}}^{t_{\rm r}} \nabla_{\boldsymbol{k}} E_{\rm C2}[\boldsymbol{k}_0 + A(\tau) - A(t_{\rm i})]d\tau, \tag{12}$$

with $t_{\rm t}$ being the tunneling instant from C1 to C2. Setting the initial crystal momentum to be $-0.6\pi/a_0$ as shown in Fig. 3(b) and the ionization time $t_{\rm i}$ at the injection instant $3.75T_{\rm L}$, Fig. 4(c) shows the dependence of harmonic energy and recombination time on the tunneling instant. It can be seen that the recombination time and energy of harmonic emission show nearly perfect match with the time-frequency analyses. Surprisingly, though emissions in the secondary plateau exhibit both positive and negative chirps, the chirps are not related to the so-called long or short trajectories in the interband dynamics of the first plateau. Actually, the positively and negatively chirped emission in the extended region is radiated by electrons from the 'general' trajectory, where the electrons that ionize earlier recombine earlier and the interval between ionization and recombination are approximately between $0.37T_{\rm L}$ and $\sim 0.6T_{\rm L}$, depending on the harmonic energy. Varying the band dispersion gives a delay between $0.1T_{\rm L}$ and $0.7T_{\rm L}$, approaching that of the short trajectory. As a matter of fact, time interval between tunneling and recombination depends on the actual band dispersion of band C2, because it determines the group velocity of re-

combining electrons, indicated by Eq. (12). The sensitivity to band dispersion, on the other hand, can be possibly applied to reconstruct the band structure of higher-lying band. It should also be noted that, though the 'general' trajectory in the second plateau is obvious under UV injection, other paths of excitation to higher-lying band can still be possible, such as direct transition from V1 to C2 under intense IR incidence, and emissions from these paths are dominated by 'short' or 'long' trajectory.

In summary, we have investigated the multiband dynamics of cut-off extension in the IR+UV scheme employing 1D SBE. Through linear scaling of cutoff intensity on injection intensity, delay sensitivity and time-dependent population difference, we solidify the foundation of the extended three-step model in describing the origin of population increase on high-lying conduction band. Surprisingly, deeper exploration into the time-frequency characteristics shows that, though both positive and negative chirps coexists during the subcycle dynamics in the first and second plateaus, the positive chirp in the first plateau is radiated by electrons that ionize later but recombine earlier while that in the second plateau is linked to electrons that tunnel earlier and recombine earlier. Our research may have implications for generation of table-top attosecond sources and hold the promise of all-optical reconstruction of band structure beyond the lowest band edge.

*Acknowledgments.* This work was supported by the National Key R&D Program of China (Grant No. 2019YFA0307703), the National Natural Science Foundation of China (Grant Nos. 12234020, 12274461, and 11904400), and the Major Research Plan of the National Natural Science Foundation of China (Grant No. 91850201).

## References

[1] Krausz F and Ivanov M 2009 *Rev. Mod. Phys.* **81** 163
[2] Corkum P B 1993 *Phys. Rev. Lett.* **71** 1994
[3] Lewenstein M, Balcou P, Ivanov M Y, L'Huillier A, and Corkum P B 1994 *Phys. Rev. A* **49** 2117
[4] Ferray M, L'Huillier A, Li X F, Lompre L A, Mainfray G, and Manus C 1988 *J. Phys. B* **21** L31
[5] McPherson A, Gibson G, Jara H, Johann U, Luk T S, McIntyre I A, Boyer K, and Rhodes C K 1987 *J. Opt. Soc. Am. B* **4** 595
[6] Paul P M, Toma E S, Breger P, Mullot G, Augé F, Balcou P, Muller H G, and Agostini P 2001 *Science* **292** 1689
[7] Hohenleutner M, Langer F, Schubert O, Knorr M, Huttner U, Koch S W, Kira M, and Huber R 2015 *Nature* **523** 572
[8] Popmintchev T, Chen M C, Popmintchev D, Arpin P, Brown S, Ališauskas S, Andriukaitis G, Balčiunas T, Mücke O D, Pugzlys A, Baltuška A, Shim B, Schrauth S E, Gaeta A, Hernández-García C, Plaja L, Becker A, Jaron-Becker A, Murnane M M, and Kapteyn H C 2012 *Science* **336** 1287
[9] Zhang B and Zhao Z X 2013 *Chin. Phys. Lett.* **30** 023202
[10] Kienberger R, Hentschel M, Uiberacker M, Spielmann C, Kitzler M, Scrinzi A, Wieland M, Westerwalbesloh T, Kleineberg U, Heinzmann U, Drescher M, and Krausz F 2002 *Science* **297** 1144
[11] Klünder K, Dahlström J M, Gisselbrecht M, Fordell T, Swoboda M, Guénot D, Johnsson P, Caillat J, Mauritsson J, Maquet A, Taïeb R, and L'Huillier A 2011 *Phys. Rev. Lett.* **106** 143002
[12] Drescher M, Hentschel M, Kienberger R, Uiberacker M, Yakovlev V, Scrinzi A, Westerwalbesloh T, Kleineberg U, Heinzmann U, and Krausz F 2002 *Nature* **419** 803
[13] Maquet A, Caillat J, and Taïeb R 2014 *J. Phys. B* **47** 204004
[14] Midorikawa K 2022 *Nat. Photon.* **16** 267
[15] Uiberacker M, Uphues T, Schultze M, Verhoef A J, Yakovlev V, Kling M F, Rauschenberger J, Kabachnik N M, Schröder H, Lezius M, Kompa K L, Muller H G, Vrakking M J J, Hendel S, Kleineberg U, Heinzmann U, Drescher M, and Krausz F 2007 *Nature* **446** 627
[16] Zhang D W, Lü Z H, Meng C, Du X Y, Zhou Z Y, Zhao Z X, and Yuan J M 2012 *Phys. Rev. Lett.* **109** 243002
[17] Huang Y D, Meng C, Wang X W, Lü Z H, Zhang D W, Chen W B, Zhao J, Yuan J M, and Zhao Z X 2015 *Phys. Rev. Lett.* **115** 123002
[18] Huang Y D, Zhao J, Shu Z, Zhu Y L, Liu J L, Dong W P, Wang X W, Lü Z H, Zhang D W, Yuan J M, Chen J, and Zhao Z X 2021 *Ultrafast Sci.* **2021** 9837107
[19] Zhao Z X 2021 *Chin. Sci. Bull.* **66** 913 (in Chinese)
[20] Dong W P, Hu H Y, and Zhao Z X 2020 *Opt. Express* **28** 22490
[21] Li J, Ren X M, Yin Y C, Zhao K, Chew A, Cheng Y, Cunningham E, Wang Y, Hu S Y, Wu Y, Chini M, and Chang Z H 2017 *Nat. Commun.* **8** 186
[22] Li J, Chew A, Hu S Y, White J, Ren X M, Han S, Yin Y C, Wang Y, Wu Y, and Chang Z H 2019 *Opt. Express* **27** 30280
[23] Ren X M, Li J, Yin Y C, Zhao K, Chew A, Wang Y, Hu S Y, Cheng Y, Cunningham E, Wu Y, Chini M, and Chang Z H 2018 *J. Opt.* **20** 023001
[24] Wang X W, Wang L, Xiao F, Zhang D W, Lü Z H, Yuan J M, and Zhao Z X 2020 *Chin. Phys. Lett.* **37** 023201
[25] Plaja L and Roso-Franco L 1992 *Phys. Rev. B* **45** 8334
[26] Faisal F H M and Kamiński J Z 1997 *Phys. Rev. A* **56** 748
[27] Liu L, Zhao J, Dong W P, Liu J L, Huang Y D, and Zhao Z X 2017 *Phys. Rev. A* **96** 053403
[28] Liu L, Zhao J, Yuan J M, and Zhao Z X 2019 *Chin. Phys. B* **28** 114205
[29] Goulielmakis E and Brabec T 2022 *Nat. Photon.* **16** 411
[30] Yu C, Jiang S C, and Lu R F 2019 *Adv. Phys.: X* **4** 1562982
[31] Jiang S C, Chen J G, Wei H, Yu C, Lu R F, and Lin C D 2018 *Phys. Rev. Lett.* **120** 253201
[32] Ghimire S, Dichiara A D, Sistrunk E, Agostini P, Dimauro L F, and Reis D A 2011 *Nat. Phys.* **7** 138
[33] Vampa G, Hammond T J, Thiré N, Schmidt B E, Légaré F, McDonald C R, Brabec T, and Corkum P B 2015 *Nature* **522** 462
[34] Vampa G, McDonald C R, Orlando G, Klug D D, Corkum P B, and Brabec T 2014 *Phys. Rev. Lett.* **113** 73901
[35] Vampa G, Lu J, You Y S, Baykusheva D R, Wu M, Liu H, Schafer K J, Gaarde M B, Reis D A, and Ghimire S 2020 *J. Phys. B* **53** 144003
[36] Ndabashimiye G, Ghimire S, Wu M, Browne D A, Schafer K J, Gaarde M B, and Reis D A 2016 *Nature* **534** 520
[37] Schultze M, Bothschafter E M, Sommer A, Holzner S, Schweinberger W, Fiess M, Hofstetter M, Kienberger R, Apalkov V, Yakovlev V S, Stockman M I, and Krausz F 2013 *Nature* **493** 75
[38] Schiffrin A, Paasch-Colberg T, Karpowicz N, Apalkov V, Gerster D, Mühlbrandt S, Korbman M, Reichert J, Schultze M, Holzner S, Barth J V, Kienberger R, Ernstorfer R, Yakovlev V S, Stockman M I, and Krausz F 2013 *Nature* **493** 70
[39] Vampa G, Hammond T J, Thiré N, Schmidt B E, Légaré F, McDonald C R, Brabec T, Klug D D, and Corkum P B 2015 *Phys. Rev. Lett.* **115** 193603
[40] Yu C, Jiang S C, Wu T, Yuan G L, Wang Z W, Jin C, and Lu R F 2018 *Phys. Rev. B* **98** 085439

[41] Lakhotia H, Kim H Y, Zhan M, Hu S, Meng S, and Goulielmakis E 2020 *Nature* **583** 55

[42] Silva R E, Jiménez-Galán Á, Amorim B, Smirnova O, and Ivanov M 2019 *Nat. Photon.* **13** 849

[43] Qian C, Yu C, Jiang S C, Zhang T, Gao J C, Shi S, Pi H Q, Weng H M, and Lu R F 2022 *Phys. Rev. X* **12** 021030

[44] Shao C, Lu H T, Zhang X, Yu C, Tohyama T, and Lu R F 2022 *Phys. Rev. Lett.* **128** 047401

[45] Nourbakhsh Z, Tancogne-Dejean N, Merdji H, and Rubio A 2021 *Phys. Rev. Appl.* **15** 014013

[46] Liu X, Zhu X S, Lan P F, Zhang X F, Wang D, Zhang Q B, and Lu P X 2017 *Phys. Rev. A* **95** 063419

[47] Li L, Lan P F, Zhu X S, Huang T F, Zhang Q B, Lein M, and Lu P X 2019 *Phys. Rev. Lett.* **122** 193901

[48] Nefedova V E, Fröhlich S, Navarrete F, Tancogne-Dejean N, Franz D, Hamdou A, Kaassamani S, Gauthier D, Nicolas R, Jargot G, Hanna M, Georges P, Ciappina M F, Thumm U, Boutu W, and Merdji H 2021 *Appl. Phys. Lett.* **118** 201103

[49] Yu C, Hansen K K, and Madsen L B 2019 *Phys. Rev. A* **99** 013435

[50] Yu C, Jiang S C, Wu T, Yuan G L, Peng Y G, Jin C, and Lu R F 2020 *Phys. Rev. B* **102** 241407

[51] Song X H, Yang S D, Zuo R X, Meier T, and Yang W F 2020 *Phys. Rev. A* **101** 033410

[52] Navarrete F, Ciappina M F, and Thumm U 2019 *Phys. Rev. A* **100** 033405

[53] Shao T J, Lü L J, Liu J Q, and Bian X B 2020 *Phys. Rev. A* **101** 053421

[54] Uzan A J, Orenstein G, Á J G, McDonald C, Silva R E F, Bruner B D, Klimkin N D, Blanchet V, Arusi-Parpar T, Krüger M, Rubtsov A N, Smirnova O, Ivanov M, Yan B, Brabec T, and Dudovich N 2020 *Nat. Photon.* **14** 183

[55] Sun N, Zhu X S, Li L, Lan P F, and Lu P X 2021 *Phys. Rev. A* **103** 053111

[56] Lang Y, Peng Z Y, Liu J L, Zhao Z X, and Ghimire S 2022 *Phys. Rev. Lett.* (accepted)

[57] Yue L and Gaarde M B 2020 *Phys. Rev. A* **101** 053411

[58] Yue L and Gaarde M B 2022 *J. Opt. Soc. Am. B* **39** 535

[59] Földi P 2017 *Phys. Rev. B* **96** 035112

[60] Peng Q F, Peng Z Y, Lang Y, Zhu Y L, Zhang D W, Lü Z H, and Zhao Z X 2022 *Chin. Phys. Lett.* **39** 053301

[61] Lindefelt U, Nilsson H E, and Hjelm M 2004 *Semicond. Sci. Technol.* **19** 1061

[62] Ghimire S and Reis D A 2019 *Nat. Phys.* **15** 10

[63] Korbman M, Yu K S, and Yakovlev V S 2013 *New J. Phys.* **15** 013006